RSC Advances

PAPER

View Article Online
View Journal | View Issue

Check for updates

Cite this: *RSC Adv.*, 2023, **13**, 17315

Ultralow-iridium content NiIr alloy derivative nanochain arrays as bifunctional electrocatalysts for overall water splitting†

Zhengyang Cai, [ab] Ping Wang, *[b] Xianglong Zhao,[c] Xiuming Bu,[b] Jiajia Zhang,[b] Yuhao Chen,[ab] Jingcheng Xu,[a] Ya Yan, [b] Aiying Chen *[a] and Xianying Wang*[b]

The development of low-cost and high-durability bifunctional electrocatalysts is of considerable importance for overall water splitting (OWS). This work reports the controlled synthesis of nickel–iridium alloy derivative nanochain array electrodes ($NiIr_x$ NCs) with fully exposed active sites that facilitated mass transfer for efficient OWS. The nanochains have a self-supported three-dimensional core–shell structure, composed of a metallic $NiIr_x$ core and a thin (5–10 nm) amorphous (hydr)oxide film as the shell (*e.g.*, $IrO_2/NiIr_x$ and $Ni(OH)_2/NiIr_x$). Interestingly, $NiIr_x$ NCs have bifunctional properties. Particularly, the oxygen evolution reaction (OER) current density (electrode geometrical area) of $NiIr_1$ NCs is four times higher than that of IrO_2 at 1.6 V *vs.* RHE. Meanwhile, its hydrogen evolution reaction (HER) overpotential at 10 mA cm^{-2} (η_{10} = 63 mV) is comparable to that of 10 wt% Pt/C. These performances may originate from the interfacial effect between the surface (hydr)oxide shell and metallic $NiIr_x$ core, which facilitates the charge transfer, along with the synergistic effect between Ni^{2+} and Ir^{4+} in the (hydr) oxide shell. Furthermore, $NiIr_1$ NCs exhibits excellent OER durability (100 h @ 200 mA cm^{-2}) and OWS durability (100 h @ 500 mA cm^{-2}) with the nanochain array structure well preserved. This work provides a promising route for developing effective bifunctional electrocatalysts for OWS applications.

Received 21st March 2023
Accepted 30th May 2023

DOI: 10.1039/d3ra01845h

rsc.li/rsc-advances

Open Access Article. Published on 08 June 2023. Downloaded on 2/19/2026 2:25:09 AM.
This article is licensed under a Creative Commons Attribution-NonCommercial 3.0 Unported Licence.

Introduction

Electrocatalysts with low-cost, high-efficiency and excellent-durability for industrial-scale overall water splitting (OWS) application are urgently required.[1–5] Especially for the anode's oxygen evolution reaction (OER), the kinetics of which is about 5 times slower than that of cathode's hydrogen evolution reaction (HER).[6–8] Platinum group metal based materials are realized as efficient electrocatalysts like iridium (Ir), ruthenium (Ru) for OER and platinum (Pt), palladium (Pd) for HER. However, their large-scale applications are limited by their scarcity and high cost.[9–11] Thus, it is necessary to develop low-cost and bifunctional electrocatalysts with facile strategies. Although, a great deal of research has been performed in order to investigate non-noble metal-based electrocatalysts for the OER and HER,[12,13] their overpotentials are still not satisfactory, and their long-term durability is usually tested at low current density, mostly less than 100 mA cm^{-2}, and these assessment criteria can't meet the requirement for industrial applications.[14–18] On the other hand, as the precious IrO_2 is considered to have excellent OER activity and durability,[19–21] researchers have devoted tremendous effort to minimizing the Ir loading on the electrode and improving its utilization through various modification strategies. For example, improving active sites exposure *via* hierarchical architecture designing,[22–24] improving noble metal atom utilization *via* single-atom electrocatalysts development,[25,26] and compounding non-noble metal elements to ensure the satisfactory durability and improving the electrocatalytic activity.[27,28] However, more research is needed to further reduce the content of noble metals to achieve a balance between high OER activity and excellent durability. In terms of HER, no matter from the DFT-calculated HER volcano plot or the experiment, it is verified that Ir is also an element with HER activity.[29–32] Therefore, it would be advantageous if an electrocatalyst with low Ir content was bifunctional for OER and HER. In addition, it is also necessary to develop high-efficiency bifunctional electrocatalysts to improve production efficiency in terms of time and cost.

Herein, we report a series of bifunctional self-supported three-dimensional core–shell structured $NiIr_x$ alloy derivative nanochain array electrodes ($NiIr_x$ NCs, x = 0, 0.01, 0.1, 0.5, 0.9, 1, 5, 10, 20, molar ratio between Ni and Ir) for efficient OWS, which were synthesized *via* a facile one-step chemical reduction

[a]*School of Materials and Chemistry, University of Shanghai for Science and Technology, 200093, Shanghai, P. R. China. E-mail: aychen@usst.edu.cn*

[b]*Energy Materials Research Center Institute of Ceramics, Chinese Academy of Sciences, 200050, Shanghai, P. R. China. E-mail: wangping@mail.sic.ac.cn; wangxianying@mail.sic.ac.cn*

[c]*School of Science, Shandong Jianzhu University, Jinan, 250101, P. R. China*

† Electronic supplementary information (ESI) available. See DOI: https://doi.org/10.1039/d3ra01845h

© 2023 The Author(s). Published by the Royal Society of Chemistry

Open Access Article. Published on 08 June 2023. Downloaded on 2/19/2026 2:25:09 AM.
This article is licensed under a Creative Commons Attribution-NonCommercial 3.0 Unported Licence.

method. The $NiIr_x$ NCs composed of a metallic $NiIr_x$ core and with a thin amorphous (hydr)oxide shell (5–10 nm) on the surface and thus forming a three-dimensional core–shell structure. The diameter of $NiIr_x$ NCs ($x \neq 0$) is significantly reduced compared to $NiIr_0$ NCs, thus resulting in a high electrochemical surface area (ECSA), which benefits the exposure of active sites, and provides a large number of mass transfer channels. In addition, the *in situ* growth of nanochains on nickel foam provides good charge transfer ability and structural stability. Benefiting from the unique three-dimensional core-shelled nanochain array architecture and interfacial effect between surface thin (hydr)oxide shell and the metallic $NiIr_x$ core (*e.g.*, $IrO_2/NiIr_x$ and $Ni(OH)_2/NiIr_x$) along with the synergistic effect between Ni^{2+} and Ir^{4+} in the (hydr)oxide shell, $NiIr_x$ NCs achieve excellent electrocatalytic OER and HER activities. Especially for $NiIr_1$ NCs its OER current density is four times higher than that of commercial IrO_2 at 1.6 V *vs.* RHE. In addition, $NiIr_1$ NCs also exhibits excellent HER activity, with a low overpotential at current density of 10 mA cm^{-2} ($\eta_{10} = 63$ mV) which is close to that of commercial 10 wt% Pt/C. Furthermore, $NiIr_1$ NCs exhibited negligible OER activity change after durability test (100 h @ 200 mA cm^{-2}) and self-supporting nanochain arrays structure was maintained after OWS long-term durability test at large current density (100 h @ 500 mA cm^{-2}). Therefore, $NiIr_1$ NCs are promising bifunctional electrocatalysts for OWS with high electrocatalytic activity, good durability and low cost. These findings would provide new opportunities for the design of industrial requirement meetable electrocatalysts with efficient bifunctional OWS performance.

Experimental section

Chemicals

The chemicals are used as received without further purification. Hydrochloric acid (HCl, AR, Adamas, China), ethanol (C_2H_5OH, ≥99.7%, Adamas, China), 2-propanol (C_3H_8O, ≥99.7%, Greagent, China), sodium citrate dehydrate ($C_6H_5Na_3O_7 \cdot 2H_2O$, ≥99.0%, Aladdin Co., China), nickel chloride hexahydrate ($NiCl_2 \cdot 6H_2O$, AR, Aladdin Co., China), dihydrogen hexachloroiridate(IV) hydrate ($H_2Cl_6Ir \cdot xH_2O$, Ir ≥ 35.0%, Adamas, China), hydrazine monohydrate (N_2H_4 H_2O, >98.0%, Aladdin Co., China), iridium(IV) oxide (IrO_2, 99.9%, Adamas, China), platinum on carbon (10 wt% Pt/C, Sigma-Aldrich, Germany), potassium hydroxide (KOH, trace metal basis 99.99%, Acros, Belgium), Nafion D-521 solution (5 wt%, Alfa Aesar, USA), Ni foam (0.5 mm in thickness, Tianjin EVS Co., China), anion exchange membrane (Fumasep® FAA-3-50) and deionized (DI) water (~18.2 MΩ cm) is used throughout all experiments.

Fabrication of nickel–iridium alloy nanochains ($NiIr_x$ NCs, x = 0, 0.01, 0.1, 0.5, 0.9, 1, 5, 10, 20)

The *in situ* growth of $NiIr_x$ NCs array on Ni foam (NF) was carried out *via* a magnetic field-assisted chemical reduction method. Typically, a piece of NF with a dimension of 3 × 3 cm^2 was cleaned with hydrochloric acid (37 wt%) to remove the surface oxide layer and rinsed with ethanol and DI water for several times sequentially. Specifically, 50 mL aqueous solutions containing different molar ratios of $H_2Cl_6Ir \cdot xH_2O$ (0, 0.01, 0.1, 0.5, 0.9, 1, 5, 10 and 20%) with a total metal atomic (Ni + Ir) concentration of 0.1 M were heated at 70 °C, followed by adding 5 wt% of $N_2H_4 \cdot H_2O$. Taking $NiIr_1$ NCs as an example, the ratio of each component in the 50 mL precursor solution is $NiCl_2 \cdot 6H_2O$ (0.099 M), $H_2Cl_6Ir \cdot xH_2O$ (0.001 M) and $Na_3C_6H_5O_7 \cdot 2H_2O$ (0.02 M). The beaker containing precursor solution was placed on a magnet, and the Ni foam at the bottom of the beaker was oriented vertically to the direction of the magnetic field lines. The reduced Ni nanoparticles will be attracted by the magnet and grow into nanochains along the direction of the magnetic field lines. This allowed the $NiIr_x$ NCs to grow perpendicular to the surface of the foam Ni. The mixture was kept at 70 °C for 60 min. The obtained $NiIr_x$ NCs were washed sequentially by ethanol and DI water and dried in vacuum overnight.

Preparation of IrO_2 and Pt/C electrodes

The control electrodes of IrO_2 and Pt/C were prepared by drop-coating catalyst ink onto NF. For example, to prepare the IrO_2 electrode, 20 mg IrO_2, 40 μL Nafion solution, 540 μL 2-propanol and 400 μL DI water were mixed together and ultrasonicated for forming a homogeneous dispersion, in which the solid content was about 2 wt%. Then, the suspension was coated onto NF, which was then dried at room temperature. The loading amount of IrO_2 and Pt/C electrode on NF was kept the same amount of 1.5 mg cm^{-2} with the $NiIr_1$ NCs.

Characterizations

The morphology and structure of the as-synthesized samples are detected with scanning electron microscopy (SEM, Zeiss Gemini 300), transmission electron microscope (TEM, FEI Tecnai F20) coupled with energy dispersive X-ray spectroscopy (EDX). The phase composition and chemical bonding nature in the samples are characterized by X-ray diffraction (XRD, D8 Advance) and X-ray photoelectron spectroscopy (XPS, Thermo fisher Scientific K-Alpha+). The Ni and Ir dissolved contents were analyzed by inductively coupled plasma-mass spectrometry (ICP-MS, Aglient 7800).

Electrochemical measurements

Electrochemical measurements are carried out on an electrochemical workstation (Ivium Technologies, Vertex.1A, The Netherlands) in a standard three-electrode system equipped with the as-prepared samples as the working electrode, a Φ6 mm graphite rod as the counter electrode, and a Hg/HgO electrode as the reference electrode. The OER and HER activities are evaluated using cyclic voltammetry (CV) and linear sweep voltammetry (LSV) methods in 1 M KOH aqueous solution. The stability tests are performed by chronopotentiometry method at a constant current density in 1 M KOH aqueous solution. Electrochemical impedance spectra (EIS) are measured at a potential of 1.53 V *vs.* RHE for OER and −0.15 V *vs.* RHE for HER from 100 kHz to 0.1 Hz with an amplitude of 10 mV. The double-layer capacitance values (C_{dl}) were obtained from CV

© 2023 The Author(s). Published by the Royal Society of Chemistry

Open Access Article. Published on 08 June 2023. Downloaded on 2/19/2026 2:25:09 AM.
This article is licensed under a Creative Commons Attribution-NonCommercial 3.0 Unported Licence.

measurements, which carried out at different scan rates (from 10 to 100 mV s^{-1}) in a potential range from 0.927 V to 1.027 V *vs.* RHE. All the measured potentials *vs.* Hg/HgO are converted to RHE by the Nernst equation ($E_{RHE} = E_{Hg/HgO} + 0.0592pH + 0.098$) and except where otherwise stated, an *iR* compensation of 90% are applied to all the CV and LSV curves.

Results and discussions

Synthesis and structural characterization

The fabrication of self-supporting $NiIr_x$ NCs on the nickel foam (NF) substrate was achieved *via* a simple one-step chemical reduction method. Typically, a precursor solution containing a desired atomic ratio of Ni and Ir was heated to 70 °C in a water bath, followed by adding a reducing agent under the vigorous stirring condition, and then the result homogeneous mixture was kept at 70 °C for 1 h. Detailed synthetic procedure is given in Experimental section. Firstly, the morphology and structure of $NiIr_x$ NCs were examined *via* scanning electron microscopy (SEM) and transmission electron microscopy (TEM) characterizations. As shown in Fig. S1a–e, g and h† the nanochains arrays of $NiIr_x$ NCs ($x = 0$, 0.01, 0.1, 0.5, 0.9, 1) are grown uniformly on Ni foam. Moreover, it can be observed from high-magnification images that the nanochains are assembled by stacking nanoparticles (Fig. 1a–d and S1†). This interconnected assembly has the potential to improve durability by preventing particle agglomeration and particle separation. However, with the increase of Ir content (for the $NiIr_x$ NCs ($x = 5$, 10, 20)), the nanoparticles were dispersed on the surface of NF and could not be stacked and assembled into nanochains (Fig. S1g and h†). This may be due to the different magnetic properties of Ni and Ir. Ni is a ferromagnetic material and has a strong magnetic property.[33] However, Ir is an antiferromagnetic material and has a weak magnetic property.[34] Therefore, when the Ir content in the precursor is low ($NiIr_x$ NCs, $x = 0.01$, 0.1, 0.5, 0.9, 1), the freshly reduced Ni nanoparticles will be attracted by the magnet and stack into nanochains along the direction of the magnetic field lines during the magnetic field-assisted chemical reduction process. This allowed the $NiIr_x$ NCs can grow perpendicular to the surface of the Ni foam. However, when the Ir content in the precursor is high ($NiIr_x$ NCs, $x = 5$, 10, 20), since the Ir nanoparticles cannot be attracted by the magnetic field, and the Ni nanoparticles are insufficient, resulting in the collapse of nanochain structure. Interestingly, when compared with $NiIr_0$ NCs, the nanochain diameter of $NiIr_1$ NCs is significantly

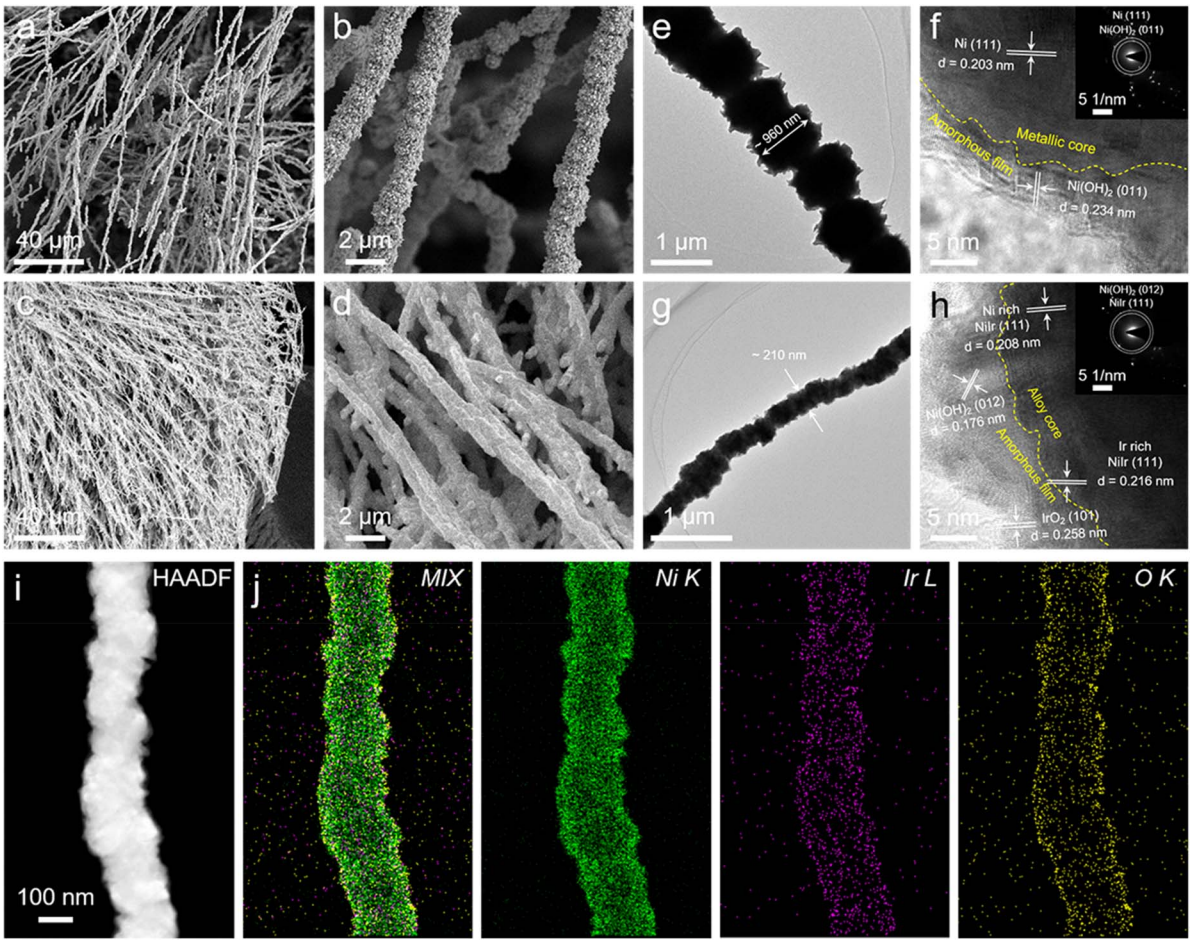

Fig. 1 SEM images with different magnifications of (a and b) $NiIr_0$ NCs, (c and d) $NiIr_1$ NCs. TEM and HRTEM images with inset SAED images of (e and f) $NiIr_0$ NCs, (g and h) $NiIr_1$ NCs. HAADF-STEM image (i) and corresponding elemental mapping of Ir, Ni and O in $NiIr_1$ NCs (j).

Open Access Article. Published on 08 June 2023. Downloaded on 2/19/2026 2:25:09 AM.
This article is licensed under a Creative Commons Attribution-NonCommercial 3.0 Unported Licence.

reduced, which will be more clearly demonstrated in the TEM results (Fig. 1e, g, S4a and c†). And a similar phenomenon was also observed in other control samples (Fig. S1a–d and S2a†). Due to more nanochains with a smaller diameter can grow per unit area, the exposure of active surface area can be facilitated greatly. The energy dispersive X-ray spectroscopy (EDX) results show that the Ni is uniformly distributed in $NiIr_0$ NCs and with a very small portion of surface oxygen (2.37 at%) (Fig. S2b†). It can be observed that the atomic ratio of Ir in $NiIr_1$ NCs is about 0.87 at%, which is close to 1 at% in the precursor, indicating a high Ir atom utilization in $NiIr_1$ NCs (Fig. S1f†). And the oxygen atomic ratio is similar to that in $NiIr_0$ NCs (2.22 at%) (Fig. S2b†). To further reveal the detailed structural information, TEM characterization was performed. It is clear that the nanochain diameter of $NiIr_1$ NCs is about 210 nm which is about 5 times smaller than that of $NiIr_0$ NCs (~960 nm) (Fig. 1e, g, S4a and c†). The well-resolved high-resolution TEM (HRTEM) images show a distinct interface in both $NiIr_0$ NCs and $NiIr_1$ NCs (yellow dashed lines in Fig. 1f and h), which formed at the junction of metallic $NiIr_x$ core and thin (5–10 nm) amorphous (hydr)oxide shell. In $NiIr_0$ NCs, the metallic Ni formed the inner core, with an interplanar spacing of 0.203 nm of Ni (111) plane can be observed. The surface layer mainly contains nickel hydroxide, and the interplanar spacing of 0.218 nm corresponds to the (011) plane of $Ni(OH)_2$ (Fig. 1f). For $NiIr_1$ NCs case (Fig. 1h), the core is composed of metallic $NiIr_x$ alloy, which is mostly Ni-rich NiIr solid solution phase with NiIr (111) planes with a plane spacing of 0.208 nm. A small fraction of the Ir-rich NiIr solid solution phase can also be observed, with NiIr (111) planes with a plane spacing of 0.216 nm. This may be due to the composition segregation near the surface.[35] In addition to $Ni(OH)_2$ ($d_{(012)} = 0.176$ nm) in the surface amorphous shell, the existence of IrO_2 ($d_{(101)} = 0.258$ nm) near the Ir-rich NiIr solid solution phase is also observed. Thus, the interface is confirmed to be formed between metallic $NiIr_x$ core and the surface (hydr) oxide shell composed of $Ni(OH)_2$ and IrO_2. The selected area electron diffraction (SAED) pattern also confirmed the existence of metallic Ni and $Ni(OH)_2$ in $NiIr_0$ NCs (Fig. S4b† and inset in Fig. 1f) and NiIr alloy and $Ni(OH)_2$ in $NiIr_1$ NCs (Fig. S4d† and inset in Fig. 1h), respectively. The elemental mapping results in Fig. 1i, j, S4e and f† for $NiIr_1$ NCs and $NiIr_0$ NCs, respectively, show that the Ni and Ir elements are uniformly distributed. A small amount of oxygen is present at the surface, corresponding to the surface amorphous (hydr)oxide layer. Therefore, the core–shell structure has been further confirmed. And from the atomic ratio results, it can be seen that the oxygen content in $NiIr_0$ NCs and $NiIr_1$ NCs is 1.99 at% and 1.56 at% (Fig. S4g and h†), respectively, and the atomic ratio of Ir in $NiIr_1$ NCs is 1.03 at%. These are consistent with the SEM-EDX results.

The crystal structure of $NiIr_x$ NCs were further examined *via* X-ray diffraction (XRD) characterization. As shown in Fig. 2a, the characteristic peaks in $NiIr_0$ NCs located at 44.7° and 52.1° are related to the (111) and (200) low-index crystal planes of Ni (JCPDS #70-0989). For $NiIr_x$ NCs ($x = 0.01$, 0.1, 0.5, 0.9, 1, 5, 10, 20), although the presence of Ir is clearly shown in the EDX results as discussed above, no diffraction peaks associated with the Ir or IrO_2 phases are observed in the XRD pattern, which suggests that Ir is distributed atomically into the Ni lattice, or

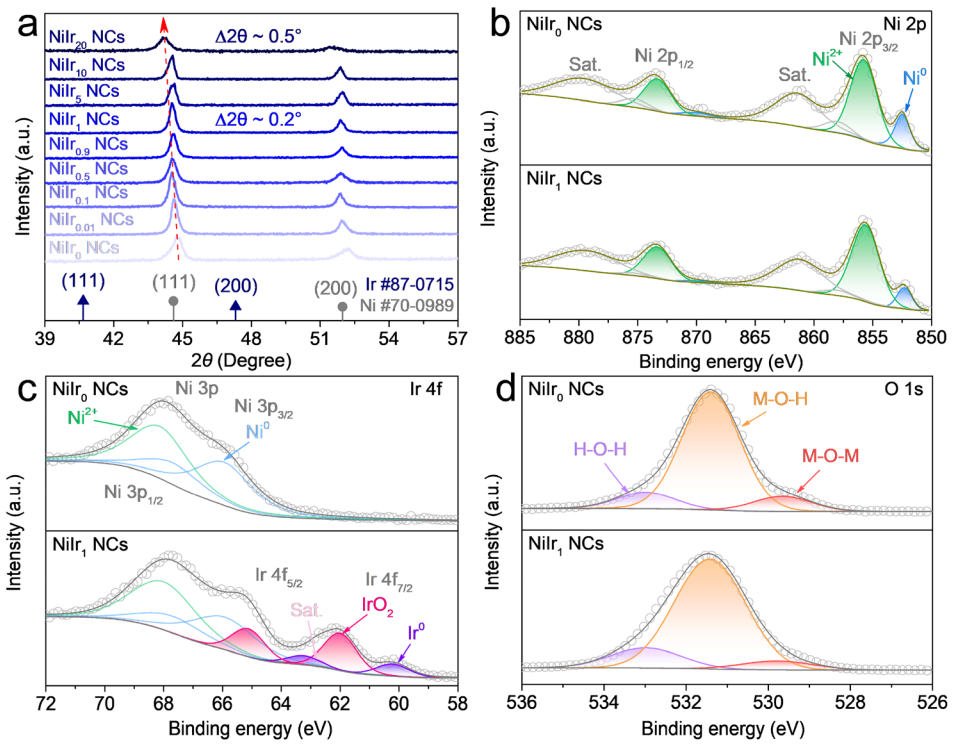

Fig. 2 (a) XRD patterns of $NiIr_x$ NCs ($x = 0$, 0.01, 0.1, 0.5, 0.9, 1, 5, 10, 20). High-resolution XPS spectra of Ni 2p (b), Ir 4f (c) and O 1s (d) of $NiIr_0$ NCs and $NiIr_1$ NCs.

© 2023 The Author(s). Published by the Royal Society of Chemistry

Open Access Article. Published on 08 June 2023. Downloaded on 2/19/2026 2:25:09 AM. This article is licensed under a Creative Commons Attribution-NonCommercial 3.0 Unported Licence.

exists in the form of IrO_2 clusters, rather than a highly ordered crystal phase. As can be clearly observed in $NiIr_x$ NCs ($x = 0.01$, 0.1, 0.5, 0.9, 1, 5, 10, 20) the diffraction peaks have negative shifts in different degrees. And negative shifts of 0.2 and 0.7° were observed in $NiIr_1$ NCs and $NiIr_{20}$ NCs, respectively. This is consistent with the fact that the volume expansion of the unit cell due to the incorporation of Ir into the Ni lattice to form the NiIr alloy solid solution, and the diffraction peak have negative shifts to lower 2θ values, which is consistent with HRTEM results.

The chemical states and surface species of $NiIr_x$ NCs ($x = 0$, 0.01, 0.1, 0.5, 0.9, 1, 10) are further investigated by X-ray photoelectron spectroscopy (XPS). As displayed in the wide-scan XPS survey in Fig. S5a,† the existence of Ni, Ir, C, and O elements is obviously observed. The binding energy positions of different species and the corresponding peak area data derived from the high-resolution XPS spectra of all elements are listed in Table S1.† As seen from the Ni 2p deconvolution spectra, a distinct Ni^{2+} phase, which belongs to $Ni(OH)_2$, can be observed in all samples, and the presence of a metallic Ni phase can also be detected (Fig. 2b and S5b†). This further proves that $Ni(OH)_2$ exists in the nanochain surface thin layer. The peaks of the metallic Ni phase are the most obvious in $NiIr_0$ NCs and $NiIr_1$ NCs, which also verifies that the thickness of the surface (hydr)oxide shell is within 10 nm, which is consistent with the TEM results. The deconvoluted XPS spectra of Ir 4f show that Ir exists in two oxidation states, Ir^{4+} and Ir^0 representing the IrO_2 and Ir metallic phases, respectively (Fig. 2c and S5c†).[36–38] The surface Ir atomic ratio obtained from XPS shows that the Ir content in $NiIr_x$ NCs ($x = 0$, 0.01, 0.1, 0.5, 0.9, 1, 10) increases with the Ir doping amount (Table S1†), which are 0.00, 0.00, 0.02, 0.02, 0.19, 0.38 and 0.75 at%, respectively. The content of IrO_2 is higher than that of the metallic Ir. This means the surface of $NiIr_x$ NCs are uniformly coated with (hydr)oxide shell, with little exposure of the internal metallic $NiIr_x$ core.

This further proves the existence of IrO_2 in the (hydr)oxide shell on the surface of nanochains. Notably, no Ir signal can be detected in $NiIr_{0.01}$ NCs and $NiIr_{0.1}$ NCs, which may be due to the fact that the doping content is below the detection limit of XPS. The Ni 3p orbital partially overlaps with the Ir 4f orbital, also showing the presence of metallic Ni and Ni^{2+}. The O 1s spectra (Fig. 2d and S5d†) further confirmed that the surface oxygen species of $NiIr_x$ NCs ($x = 0$, 0.01, 0.1, 0.5, 0.9, 1, 10) are mainly in the form of M–O–H (M = Ni) species[39–41] with a low amount of M–O–M species (M = Ni and Ir) in the $Ni(OH)_2$ and IrO_2 lattice.[42–44]

Electrocatalytic activity toward OER, HER and OWS

The electrocatalytic performance of prepared $NiIr_x$ NCs ($x = 0$, 0.01, 0.1, 0.5, 0.9, 1, 5, 10, 20) was investigated in an electrolyte (1 M KOH) with a standard three-electrode system. As shown in the cyclic voltammetry (CV) curves, the OER overpotential plot at a current density of 10 mA cm^{-2} (η_{10}) (Fig. 3a, S6a and c†), with the increase of Ir content in $NiIr_x$ NCs, η_{10} has a trend with great decrease first and then slowly increase. It is worth noting that since the SEM results show that the nanochains cannot grow well in $NiIr_x$ NCs ($x = 5$, 10, 20), the reason for the better performance when $x = 5$, 10, 20 may come from the increase of Ir content, which has higher intrinsic activity than Ni, rather than the exposure of more active sites by the nanochain array since the nanoparticles were dispersed on the surface of NF as discussed in SEM results. But such a high Ir content will cause a cost limit for large-scale applications. Therefore, $NiIr_1$ NC was selected as the optimal sample. Interestingly, the η_{10} of $NiIr_1$ NCs (253 mV) is significantly lower than that of $NiIr_0$ NCs (363 mV) and also better than that of commercial IrO_2 (300 mV). In addition, the current density of $NiIr_1$ NCs at 1.6 V *vs.* RHE (189 mA cm^{-2}) is four times higher than that of IrO_2 (44 mA cm^{-2}). This excellent OER activity may be attributed to both the interfacial effect between the surface $Ni(OH)_2/IrO_2$ thin film and the beneath metallic $NiIr_x$ core, which facilitates the charge transfer from the (hydr)oxide shell to the metallic $NiIr_x$ core, and the synergistic effect between Ni^{2+} and Ir^{4+} in the (hydr) oxide shell, which can regulate the local electronic configuration to optimize the adsorption and desorption energy of the OER intermediates.[45–50] In contrast, although there is also an interface formed by $Ni(OH)_2$ and Ni in $NiIr_0$ NCs, Ir is missing and thus results in a lack of synergistic enhancement and the poor conductivity of $Ni(OH)_2$.[45,48] And similar reasons can also be found in IrO_2 where the synergistic effect between Ni and Ir and the interface effect between IrO_2/Ir are both absent. Since the OER mechanism is a complex four-electron transfer step, the Tafel slope is employed to theoretically analyze the rate-determining step (RDS) of the reaction on electrocatalysts. As shown in Fig. 3b and S6f,† $NiIr_1$ NCs have a Tafel slope of 74.9 mV dec^{-1}, which is smaller than that of $NiIr_0$ NCs (75.8 mV dec^{-1}) and IrO_2 (109.4 mV dec^{-1}). The other $NiIr_x$ NCs control groups have Tafel slopes close to 60 mV dec^{-1} (Fig. S6b and f†), which indicates that the OER process on $NiIr_x$ NCs has faster charge transfer and the RDS is the second step (*OH to *O).[51,52] The RDS on IrO_2 is the first electron transfer reaction.[51]

In addition to the interfacial effect, the fast charge transfer on $NiIr_x$ NCs also benefits from the *in situ* grown self-supporting structure, which makes a strong combination between nanochains and the support NF. Furthermore, since the η_{10} of $NiIr_0$ NCs is much larger than that of $NiIr_1$ NCs, the Nyquist plot shows that its OER charge transfer resistance (R_{ct}) is much larger than that of $NiIr_1$ NCs (Fig. 3c), which confirms the fast charge transfer on $NiIr_1$ NCs. $NiIr_1$ NCs also shows excellent OER durability with negligible potential change at current density of 200 mA cm^{-2} for 100 h (Fig. 3i). And the CV curves tested before and after the durability test overlap well in the OER part, except that the redox peaks belonging to $Ni^{2+/3+}$ at 1.4 V *vs.* RHE are enhanced and shifted to the anodic direction after the durability test. This is due to the oxidation of Ni and the aging effect of $Ni(OH)_2$ on the surface of the nanochain in the alkaline environment, which partially converts the redox couple of α-$Ni(OH)_2$/γ-NiOOH to β-$Ni(OH)_2$/β-NiOOH (Fig. 3h).[53,54]

To investigate the bifunctional properties of the prepared samples, the electrochemical HER test was also performed. As shown in the CV curve and η_{10} plot of HER (Fig. 3d, S6d and c†). Compared to $NiIr_0$ NCs, the HER activities of $NiIr_x$ NCs ($x =$

Open Access Article. Published on 08 June 2023. Downloaded on 2/19/2026 2:25:09 AM.
This article is licensed under a Creative Commons Attribution-NonCommercial 3.0 Unported Licence.

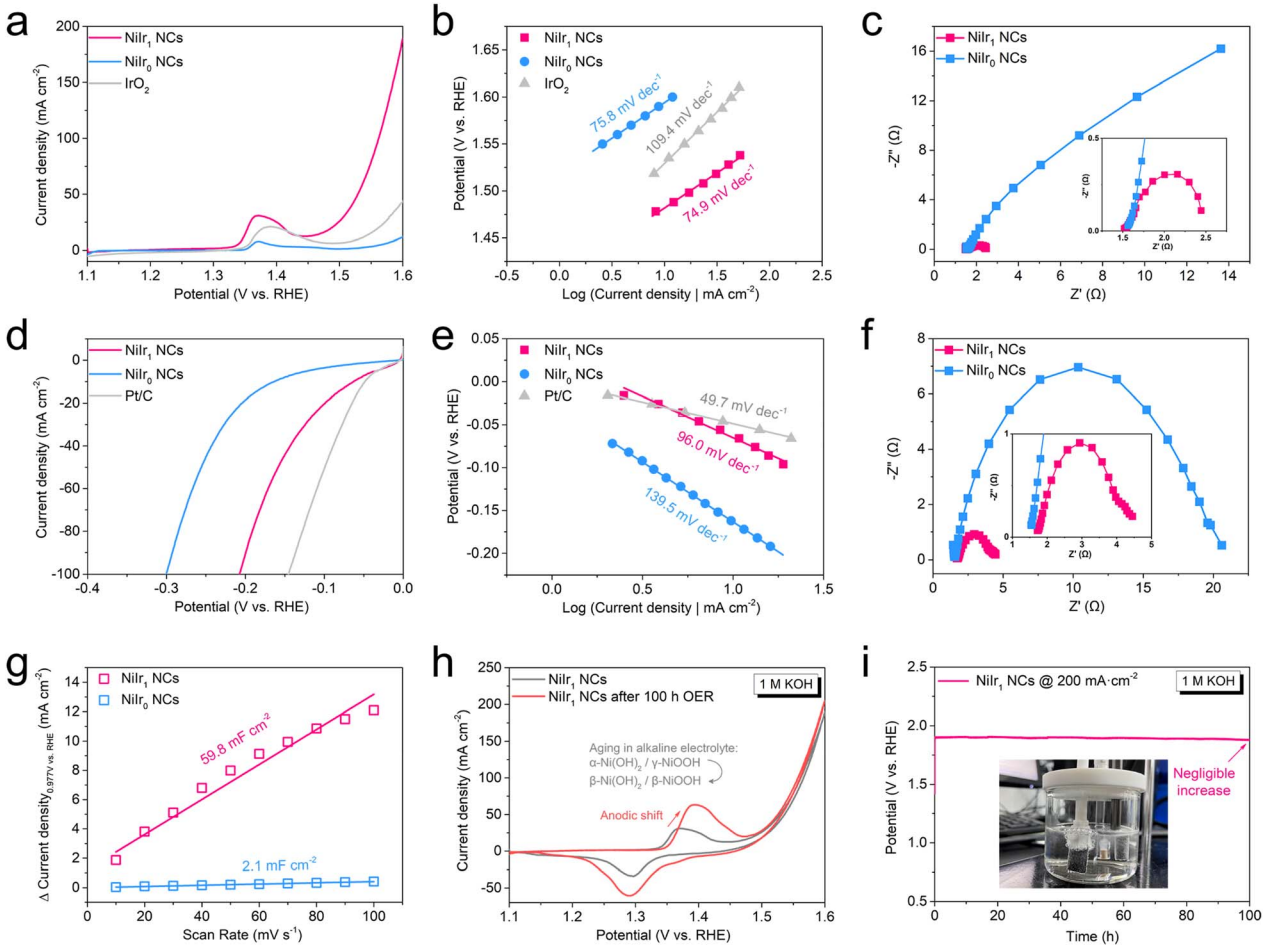

Fig. 3 Electrochemical characterization in 1 M KOH electrolyte. (a) OER LSV curves of $NiIr_0$ NCs, $NiIr_1$ NCs and IrO_2 at a scan rate of 5 mV s^{-1}. (b) The corresponding OER Tafel slopes. (c) OER Nyquist plots. (d) HER LSV curves of $NiIr_0$ NCs, $NiIr_1$ NCs and Pt/C at a scan rate of 5 mV s^{-1}. (e) The corresponding HER Tafel slopes. (f) HER Nyquist plots. (g) Calculations of C_{dl} for $NiIr_0$ NCs and $NiIr_1$ NCs. (h) OER CV curves before and after the durability test at a scan rate of 5 mV s^{-1}. (i) OER chronopotentiometry test of $NiIr_1$ NCs and the inset shows the three-electrode system used for the test.

0.01, 0.1, 0.5, 0.9, 1, 5, 10, 20) were improved. And the η_{10} of $NiIr_1$ NCs (63 mV) is comparable to that of commercial 10 wt% Pt/C (49 mV). Interestingly, even trace amounts of Ir in NiIr alloy ($NiIr_{0.01}$ NCs) can dramatically improve the HER activity. In addition, the HER activity of $NiIr_x$ NCs ($x = 0.01, 0.1, 0.5, 0.9, 1$) was observed to slowly increase with increasing Ir content. But when $x = 5$, 10 and 20, which is different from the OER case, the activity of $NiIr_x$ NCs decreased significantly. The η_{10} of $NiIr_5$ NCs, $NiIr_{10}$ NCs and $NiIr_{20}$ NCs are 109, 86 and 86 mV, respectively. These findings indicate that Ir does not play a dominant role in the promotion of HER activity of $NiIr_x$ NCs. And this will be explained further below. The HER Tafel slopes of $NiIr_x$ NCs ($x = 0$, 0.01, 0.1, 0.5, 0.9, 1, 5, 10, 20) are all close to 120 mV dec^{-1} (Fig. 3e, S6e and f†), indicating that the Volmer step acts as the RDS.[55] Notably, the estimated Tafel slope of $NiIr_1$ NCs (96 mV dec^{-1}) is significantly lower than those of $NiIr_0$ NCs (139.5 mV dec^{-1}) and $NiIr_5$ NCs (142.7 mV dec^{-1}). Since the Ir content does not dominate the HER, the large difference of the Tafel slope is most likely due to the difference in mass transfer rate, which affects the intermediate adsorption of the Volmer step. And $NiIr_1$ NCs also had a smaller HER R_{ct} than that of $NiIr_0$ NCs (Fig. 3f). It can be seen from the insets of Fig. 3c and f that the solution resistance (R_s) for OER and HER are similar (about 1.5 Ω).

To further reveal the origin of the high HER activity, we characterized the ECSA of $NiIr_0$ NCs and $NiIr_1$ NCs (Fig. S7†). The results show that the double-layer capacitance (C_{dl}) of $NiIr_1$ NCs (59.8 mF cm^{-2}) is nearly 30 times higher than that of $NiIr_0$ NCs (2.1 mF cm^{-2}) (Fig. 3g). And C_{dl} is proportional to ECSA. As predicted from the SEM and TEM morphologies, the smaller nanochain diameter of $NiIr_1$ NCs enables more nanochains to grow per unit area, resulting in a larger ECSA. In addition, the presence of Ir makes the nanochains grow thinner, so the HER η_{10} of $NiIr_{0.01}$ NCs decreases abruptly compared with $NiIr_0$ NCs. A further comparison of OER and HER performance on recently reported low noble-metal-based electrocatalysts is given in Table S2.†

By a combination of the outstanding OER and HER performance of $NiIr_1$ NCs, benefiting from the unique self-supporting structure of nanochain arrays and reinforced with (hydr)oxide/

© 2023 The Author(s). Published by the Royal Society of Chemistry

Open Access Article. Published on 08 June 2023. Downloaded on 2/19/2026 2:25:09 AM.
This article is licensed under a Creative Commons Attribution-NonCommercial 3.0 Unported Licence.

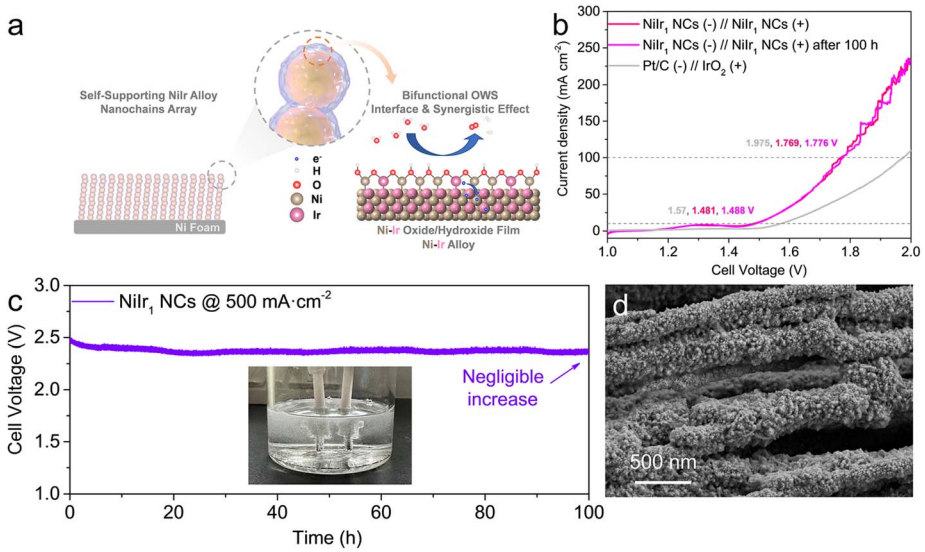

Fig. 4 (a) Schematic illustration of the nanochains array electrode with self-supported three-dimensional core–shell structure and the bifunctional OWS process. (b) OWS LSV curves before and after the durability test at a scan rate of 5 mV s^{-1}. (c) OWS chronopotentiometry test of $NiIr_1$ NCs (−)//$NiIr_1$ NCs (+) electrode pair the inset shows the two-electrode configuration used for the tests. (d) High magnification SEM image of $NiIr_1$ NCs serves as anode after 100 h OER process.

metal interfacial effect and the synergistic effect between Ni and Ir (Fig. 4a), we tested the OWS performance in a two-electrode configuration using $NiIr_1$ NCs as both the anode and cathode. As shown in Fig. 4b, the $NiIr_1$ NCs//$NiIr_1$ NCs electrode pair exhibited good OWS performance of small cell voltages of 1.481 and 1.769 V to deliver current densities of 10 and 100 mA cm^{-2}, respectively. These cell voltages outperform the Pt/C//IrO_2 electrode pair, which needs 1.570 and 1.975 V to achieve 10 and 100 mA cm^{-2}, respectively. To eliminate the influence of side reactions such as oxygen reduction reaction (ORR) and hydrogen oxidation reaction (HOR), we also performed OWS tests of the $NiIr_1$ NCs//$NiIr_1$ NCs electrode pair in an H-type electrolysis cell separated by an anion exchange membrane (Fig. S8†). The results showed that its OWS activity has no significant difference with that in a normal electrolysis cell. It is worth noting that in a normal electrolysis cell, the current fluctuation in the high potential region due to gas diffusion is alleviated in the H-type electrolysis cell.[56,57] More importantly, a negligible increase in cell voltage can be observed after 100 h durability test at a large current density of 500 mA cm^{-2} (Fig. 4c). In addition, as shown in Fig. 4b that the overpotentials achieved from LSV curves of OWS before and after durability testing only has a slight increase of ~7 mV for both 10 and 100 mA cm^{-2}, which is within the error range. From the SEM images of $NiIr_1$ NCs which were employed as anode after the durability test (Fig. S3a† and 4d), it can be seen that the self-supporting nanochain arrays are well preserved, the high magnification image shows the surface of the nanochain becomes rough (Fig. 4d), which may be due to the oxidation of Ni and the aging effect of $Ni(OH)_2$ during the OER process as discussed above. And according to the EDX analysis, the atomic ratio of O after the durability test was increased to 6.25 at% (Fig. S3†), which is higher than that of freshly prepared (2.22 at%). Furthermore, the ICP-MS results (Table S3†) of the electrolyte after 100 h OWS stability test showed that only trace amounts of Ni (58.3 ppb) and Ir (1.6 ppb) ions were present in the electrolyte, further demonstrating the excellent electrochemical stability of $NiIr_1$ NCs.

Conclusions

In summary, this work highlights the designs of a self-supporting ultralow-iridium containing $NiIr_x$ NCs with three-dimensional core–shell structure for efficient OWS. This unique structure has high ECSA, thus the active sites can be fully exposed and facilitate the mass transfer. And the *in situ*-growth of alloy nanochain arrays also provide high structural stability and good conductivity. In addition, $NiIr_x$ NCs have bifunctional properties that can not only promote the OER activity, but also the HER. Especially, the OER activity (electrode geometrical area) of $NiIr_1$ NCs is four times higher than that of commercial IrO_2 at 1.6 V *vs.* RHE, and the HER η_{10} (63 mV) is comparable to that of 10 wt% Pt/C. A thin amorphous (hydr)oxide shell (5–10 nm) can arouse the interfacial effect with the metallic $NiIr_x$ core (*e.g.*, $IrO_2/NiIr_x$ and $Ni(OH)_2/NiIr_x$). And combining with the synergistic effect between Ni^{2+} and Ir^{4+} in the (hydr)oxide shell, the excellent electrocatalytic can be achieved. Furthermore, $NiIr_1$ NCs exhibited excellent OER durability (100 h @ 200 mA cm^{-2}) and excellent OWS durability (100 h @ 500 mA cm^{-2}). These findings represent a possible advance towards the low-cost, high-efficiency, and high-durability bifunctional electrocatalysts for large-scale OWS applications.

Conflicts of interest

There are no conflicts to declare.

© 2023 The Author(s). Published by the Royal Society of Chemistry

Open Access Article. Published on 08 June 2023. Downloaded on 2/19/2026 2:25:09 AM. This article is licensed under a Creative Commons Attribution-NonCommercial 3.0 Unported Licence.

Acknowledgements

The work was financially supported by the Carbon Peak & Carbon Neutrality Project (Grant Number: 21DZ1207900). The National Natural Science Foundation of China (Grant Number: 21902011). The Natural Science Foundation of Shanghai (Grant Number: 22ZR1471900). The Shanghai Qimingxing Project (Grant Number: 22QA1410300).

Notes and references

1 S. Chu and A. Majumdar, *Nature*, 2012, **488**, 294–303.
2 C. Hu, L. Zhang and J. Gong, *Energy Environ. Sci.*, 2019, **12**, 2620–2645.
3 S. Sultan, J. N. Tiwari, A. N. Singh, S. Zhumagali, M. Ha, C. W. Myung, P. Thangavel and K. S. Kim, *Adv. Energy Mater.*, 2019, **9**, 1900624.
4 S. Chandrasekaran, M. Khandelwal, F. Dayong, L. Sui, J. S. Chung, R. D. K. Misra, P. Yin, E. J. Kim, W. Kim, A. Vanchiappan, Y. Liu, S. H. Hur, H. Zhang and C. Bowen, *Adv. Energy Mater.*, 2022, **12**, 2200409.
5 C. Pang, X. Ma, Y. Wu, S. Li, Z. Xu, M. Wang and X. Zhu, *RSC Adv.*, 2022, **12**, 22931–22938.
6 S. M. Alia, B. Rasimick, C. Ngo, K. Neyerlin, S. S. Kocha, S. Pylypenko, H. Xu and B. S. Pivovar, *J. Electrochem. Soc.*, 2016, **163**, F3105.
7 S. M. Alia, S. Shulda, C. Ngo, S. Pylypenko and B. S. Pivovar, *ACS Catal.*, 2018, **8**, 2111–2120.
8 K. Neyerlin, W. Gu, J. Jorne and H. A. Gasteiger, *J. Electrochem. Soc.*, 2007, **154**, B631.
9 P. Farràs, P. Strasser and A. J. Cowan, *Joule*, 2021, **5**, 1921–1923.
10 S. A. Grigoriev, V. N. Fateev, D. G. Bessarabov and P. Millet, *Int. J. Hydrogen Energy*, 2020, **45**, 26036–26058.
11 Z.-Y. Yu, Y. Duan, X.-Y. Feng, X. Yu, M.-R. Gao and S.-H. Yu, *Adv. Mater.*, 2021, **33**, 2007100.
12 S. Chandrasekaran, D. Ma, Y. Ge, L. Deng, C. Bowen, J. Roscow, Y. Zhang, Z. Lin, R. D. K. Misra, J. Li, P. Zhang and H. Zhang, *Nano Energy*, 2020, **77**, 105080.
13 R. Ramachandran, T.-W. Chen, P. Veerakumar, G. Anushya, S.-M. Chen, R. Kannan, V. Mariyappan, S. Chitra, N. Ponmurugaraj and M. Boominathan, *RSC Adv.*, 2022, **12**, 28227–28244.
14 G. Fu and J.-M. Lee, *J. Mater. Chem. A*, 2019, **7**, 9386–9405.
15 A. Parra-Puerto, K. L. Ng, K. Fahy, A. E. Goode, M. P. Ryan and A. Kucernak, *ACS Catal.*, 2019, **9**, 11515–11529.
16 D. S. Raja, X.-F. Chuah and S.-Y. Lu, *Adv. Energy Mater.*, 2018, **8**, 1801065.
17 F. Zheng, W. Zhang, X. Zhang, Y. Zhang and W. Chen, *Adv. Funct. Mater.*, 2021, **31**, 2103318.
18 J. Zhou, Y. Wang, X. Su, S. Gu, R. Liu, Y. Huang, S. Yan, J. Li and S. Zhang, *Energy Environ. Sci.*, 2019, **12**, 739–746.
19 S. Cherevko, S. Geiger, O. Kasian, N. Kulyk, J.-P. Grote, A. Savan, B. R. Shrestha, S. Merzlikin, B. Breitbach, A. Ludwig and K. J. J. Mayrhofer, *Catal. Today*, 2016, **262**, 170–180.
20 R. V. Genova-Koleva, F. Alcaide, G. Álvarez, P. L. Cabot, H.-J. Grande, M. V. Martínez-Huerta and O. Miguel, *J. Energy Chem.*, 2019, **34**, 227–239.
21 R. Li, H. Wang, F. Hu, K. C. Chan, X. Liu, Z. Lu, J. Wang, Z. Li, L. Zeng, Y. Li, X. Wu and Y. Xiong, *Nat. Commun.*, 2021, **12**, 3540.
22 Z. Cui and R. Qi, *Appl. Surf. Sci.*, 2021, **554**, 149591.
23 R. Samanta, P. Panda, R. Mishra and S. Barman, *Energy Fuels*, 2022, **36**, 1015–1026.
24 X. Zhao, Y. Chang, J. Ji, J. Jia and M. Jia, *RSC Adv.*, 2021, **11**, 33179–33185.
25 W.-H. Lai, L.-F. Zhang, W.-B. Hua, S. Indris, Z.-C. Yan, Z. Hu, B. Zhang, Y. Liu, L. Wang, M. Liu, R. Liu, Y.-X. Wang, J.-Z. Wang, Z. Hu, H.-K. Liu, S.-L. Chou and S.-X. Dou, *Angew. Chem., Int. Ed.*, 2019, **58**, 11868–11873.
26 Q. Wang, X. Huang, Z. L. Zhao, M. Wang, B. Xiang, J. Li, Z. Feng, H. Xu and M. Gu, *J. Am. Chem. Soc.*, 2020, **142**, 7425–7433.
27 J. Liu, J. Xiao, Z. Wang, H. Yuan, Z. Lu, B. Luo, E. Tian and G. I. N. Waterhouse, *ACS Catal.*, 2021, **11**, 5386–5395.
28 X. Yang, Y. Liu, R. Guo and J. Xiao, *Chem. Rec.*, 2022, e202200176.
29 Y. Tong, H. Mao, Q. Sun, P. Chen, F. Yan and J. Liu, *ChemCatChem*, 2020, **12**, 5720–5726.
30 S. Trasatti, *J. Electroanal. Chem. Interfacial Electrochem.*, 1972, **39**, 163–184.
31 Q. Wang, C.-Q. Xu, W. Liu, S.-F. Hung, H. B. Yang, J. Gao, W. Cai, H. M. Chen, J. Li and B. Liu, *Nat. Commun.*, 2020, **11**, 4246.
32 Z.-J. Wang, M.-X. Li, J.-H. Yu, X.-B. Ge, Y.-H. Liu and W.-H. Wang, *Adv. Mater.*, 2020, **32**, 1906384.
33 P. Huang, P. Zhang, S. Xu, H. Wang, X. Zhang and H. Zhang, *Nanoscale*, 2020, **12**, 2309–2327.
34 A. Hirohata, T. Huminiuc, J. Sinclair, H. Wu, M. Samiepour, G. Vallejo-Fernandez, K. O'Grady, J. Balluf, M. Meinert, G. Reiss, E. Simon, S. Khmelevskyi, L. Szunyogh, R. Y. Díaz, U. Nowak, T. Tsuchiya, T. Sugiyama, T. Kubota, K. Takanashi, N. Inami and K. Ono, *J. Phys. D: Appl. Phys.*, 2017, **50**, 443001.
35 F. Godínez-Salomón, L. Albiter, S. M. Alia, B. S. Pivovar, L. E. Camacho-Forero, P. B. Balbuena, R. Mendoza-Cruz, M. J. Arellano-Jimenez and C. P. Rhodes, *ACS Catal.*, 2018, **8**, 10498–10520.
36 P. A. Zhdan, G. K. Boreskov, W. F. Egelhoff and W. H. Weinberg, *Surf. Sci.*, 1976, **61**, 377–390.
37 X. Zhou, I. Hwang, O. Tomanec, D. Fehn, A. Mazare, R. Zboril, K. Meyer and P. Schmuki, *Adv. Funct. Mater.*, 2021, **31**, 2102843.
38 R. Badam, M. Hara, H.-H. Huang and M. Yoshimura, *Int. J. Hydrogen Energy*, 2018, **43**, 18095–18104.
39 A. N. Mansour, *Surf. Sci. Spectra*, 1994, **3**, 239–246.
40 A. N. Mansour and C. A. Melendres, *Surf. Sci. Spectra*, 1994, **3**, 255–262.
41 X. Yan, L. Tian and X. Chen, *J. Power Sources*, 2015, **300**, 336–343.
42 S. J. Freakley, J. Ruiz-Esquius and D. J. Morgan, *Surf. Interface Anal.*, 2017, **49**, 794–799.

© 2023 The Author(s). Published by the Royal Society of Chemistry

Open Access Article. Published on 08 June 2023. Downloaded on 2/19/2026 2:25:09 AM.
This article is licensed under a Creative Commons Attribution-NonCommercial 3.0 Unported Licence.

43 Y. Sun, Y. Li, S. You, X. Li, Y. Zhang, Z. Cai, M. Liu, N. Ren and J. Zou, *Chem. Eng. J.*, 2021, **424**, 130460.
44 F.-F. Zhang, C.-Q. Cheng, J.-Q. Wang, L. Shang, Y. Feng, Y. Zhang, J. Mao, Q.-J. Guo, Y.-M. Xie and C.-K. Dong, *ACS Energy Lett.*, 2021, **6**, 1588–1595.
45 M. Bernt, C. Schramm, J. Schröter, C. Gebauer, J. Byrknes, C. Eickes and H. A. Gasteiger, *J. Electrochem. Soc.*, 2021, **168**, 084513.
46 K. Conder, *Electronic and ionic conductivity in metal oxides*, Paul Scherrer Institute, Switzerland, 2012, pp. 1–44.
47 Z. Liu, G. Wang, J. Guo, S. Wang and S.-q. Zang, *Nano Res.*, 2023, **16**, 334–342.
48 S. A. Mahmoud, S. M. Al-Shomar and A. A. Akl, *Adv. Condens. Matter Phys.*, 2010, **2010**, 518209.
49 Y. Xu, M. Liu, M. Wang, T. Ren, K. Ren, Z. Wang, X. Li, L. Wang and H. Wang, *Appl. Catal., B*, 2022, **300**, 120753.
50 H. You, D. Wu, D. Si, M. Cao, F. Sun, H. Zhang, H. Wang, T.-F. Liu and R. Cao, *J. Am. Chem. Soc.*, 2022, **144**, 9254–9263.
51 N.-T. Suen, S.-F. Hung, Q. Quan, N. Zhang, Y.-J. Xu and H. M. Chen, *Chem. Soc. Rev.*, 2017, **46**, 337–365.
52 L. Tang, T. Fan, Z. Chen, J. Tian, H. Guo, M. Peng, F. Zuo, X. Fu, M. Li, Y. Bu, Y. Luo, J. Li and Y. Sun, *Chem. Eng. J.*, 2021, **417**, 129324.
53 S. Klaus, Y. Cai, M. W. Louie, L. Trotochaud and A. T. Bell, *J. Phys. Chem. C*, 2015, **119**, 7243–7254.
54 M. W. Louie and A. T. Bell, *J. Am. Chem. Soc.*, 2013, **135**, 12329–12337.
55 C. G. Morales-Guio, L.-A. Stern and X. Hu, *Chem. Soc. Rev.*, 2014, **43**, 6555–6569.
56 B. Bernard, S. Huaneng, P. Sivakumar and L. Vladimir, in *Electrolysis*, ed. L. Vladimir and K. Janis, IntechOpen, Rijeka, 2012, ch. 3, DOI: 10.5772/52947.
57 X. Xie, L. Du, L. Yan, S. Park, Y. Qiu, J. Sokolowski, W. Wang and Y. Shao, *Adv. Funct. Mater.*, 2022, **32**, 2110036.